A Hybrid Quadrotor with a Passively Reconfigurable Wheeled Leg Capable of Robust Terrestrial Maneuvers

Size Yu[1], Bingxuan Pu[1], Kaixu Dong[1], Songnan Bai[1] and Pakpong Chirarattananon[1,2], *Member, IEEE*

Abstract—We present a hybrid aerial-ground robot that combines the versatility of a quadcopter with enhanced terrestrial mobility. The vehicle features a passive, reconfigurable single wheeled leg, enabling seamless transitions between flight and two ground modes: a stable stance and a dynamic cruising configuration. The cruising mode exhibits exceptional turning performance, achieving a centrifugal acceleration of $0.55g$, over 30% higher than previous records, due to an inherent yaw stabilization effect. This mechanism also reduces control effort and enhances roll stability, enabling reliable navigation on irregular surfaces. While this passive design achieves structural simplicity, it trades off power efficiency for enhanced maneuverability. We provide a comprehensive analysis of the system's dynamics and experimentally demonstrate agile movements across various scenarios.

Index Terms—Aerial systems: mechanics and control, wheeled robots, aerial systems: Applications.

I. INTRODUCTION

MICRO Aerial Vehicles (MAVs) have emerged as versatile platforms for a wide range of applications, such as payload transport [1], environment monitoring [2], and surveillance [3]. However, the deployment of MAVs in urban or cluttered spaces still presents challenges related to power [4], collision avoidance [5], [6], and safe operations around humans. To address these issues, researchers have been exploring hybrid locomotion strategies that combine aerial capabilities with ground-based mobility by augmenting MAVs with legs or wheels, permitting the robots to avoid aerial collisions and crashes.

Equipping MAVs with legs offers a promising solution for navigating uneven terrain and overcoming small obstacles. Legged quadcopters can be categorized into passive designs [7]–[9], which use the existing propulsion system for ground locomotion, and active designs [10], which incorporate extra actuators for more complex movements. Passive leg designs achieve simplicity but may struggle with control, speed, and maneuverability [7]. Active legged systems offer more versatile locomotion but at the cost of mechanical complexity and increased weight. Moreover, legged hybrid MAVs tend to be less agile and maneuverable in their ground locomotion.

Wheeled MAVs are often superior in terms of agility and efficiency for ground locomotion. While some designs incorporate active wheel mechanisms for enhanced control [11]–[15], the majority employ passive mechanisms, striking a balance between simplicity and performance. These designs can be broadly classified into two categories: rolling cages and small wheel attachments. Rolling cage designs, such as [16]–[19], encapsulate the MAV within a protective frame functioning as large wheels. This approach offers robustness to surface irregularities and impact resistance but often sacrifices some agility, particularly in fast or tight turning maneuvers. Small wheel configurations, exemplified by [20], [21], often prioritize maneuverability and/or compact design, allowing for more dynamic movements on smooth, flat surfaces, and in artificial environments. However, these systems may struggle with stability on uneven terrain. Addressing these limitations is crucial for expanding the practical applications of wheeled MAVs in real-world, variable environments.

To address the limitations of existing legged and wheeled MAV designs, we propose a novel hybrid quadrotor equipped with a passively reconfigurable wheeled leg capable of robust terrestrial maneuvers. As presented in Fig. 1(a)-(c) and the Supplementary Video, our design integrates a lightweight and compact wheeled leg structure with a conventional quadcopter, offering maneuverability and robustness on uneven terrain. The key innovation lies in the passive single-degree-of-freedom revolute joint that allows the leg to reconfigure between two modes: a standing mode for stable monitoring and a cruising mode for dynamic ground locomotion. This passive design achieves high structural simplicity but requires relatively high thrust for ground locomotion, presenting a balance between system complexity and power efficiency.

The cruising mode of our design introduces a unique passive yaw rate stability mechanism. By positioning the wheel behind the robot's center of mass, we create a self-stabilizing effect that significantly enhances turning performance. As illustrated in Fig. 1(e), we present a comparison of existing works [14], [19], [21], [22] that provide sufficient data for calculating the normalized centrifugal acceleration $\bar{a}_c$, a metric for evaluating
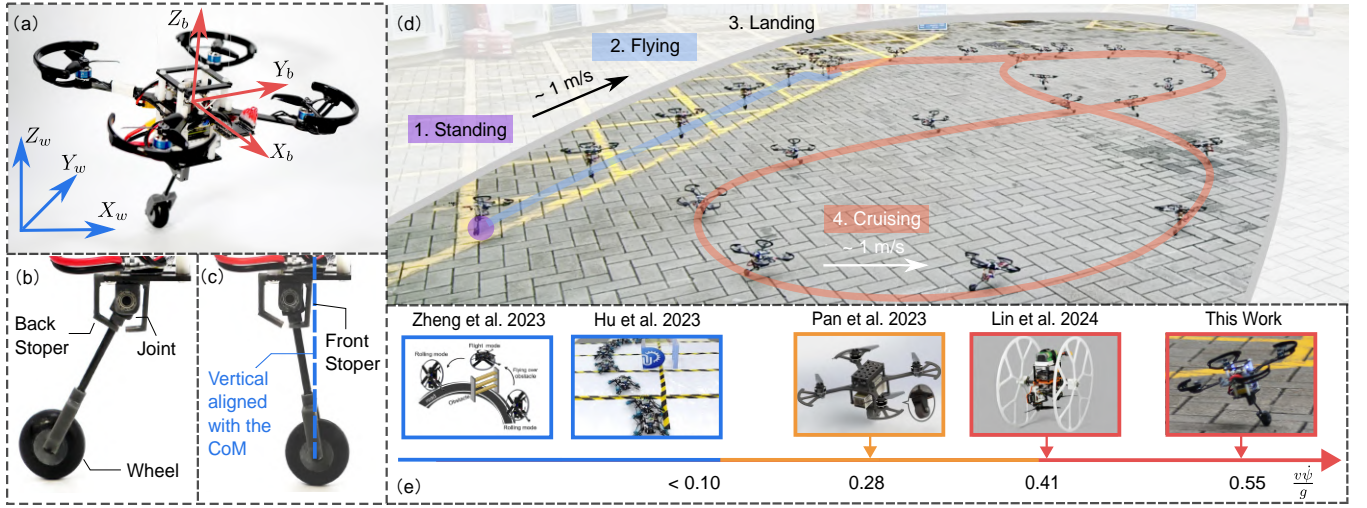
Fig. 1. Overview of the robot with a passively reconfigurable wheeled leg. (a) Close-up photo of the robot. (b) Leg configuration in cruising mode. (c) Leg in standing mode. (d) Image of the hybrid robot operating in the terrestrial and aerial modes outdoors. (e) Comparison of the normalized centrifugal acceleration ($\bar{a}_c = v\dot{\psi}/g$) of the proposed robot with existing robots [14], [19], [21], [22] The agile turning ability of the proposed vehicle is enabled by the leg mechanism and its associated passive yaw rate stability. Note that the turning radii from [21] and [19] are estimated from their trajectories.

fast turning performance. Our robot achieves a remarkable $\bar{a}_c$ value of 0.55. This performance surpasses the previous record by over 30%. The passive stability allows our robot to robustly achieve sharp turns and agile maneuvers.

In addition, we demonstrate that passive yaw rate stability reduces the control effort as well as improves roll stability. As a consequence, the passively hinged leg allows the robot to deal with surface irregularities, even when traversing small steps or bumps. This capability ensures reliable operation in diverse environments, extending the practical applications of MAVs beyond smooth and flat terrains as seen in Fig. 1(d).

The remainder of this paper is organized as follows: Section II details the mechanical design, including the passively reconfigurable wheeled leg. Section III presents the aerial and terrestrial dynamics of the robot. Section IV discusses the benefits of our reconfigurable leg design, emphasizing its passive yaw rate stability and robustness in cruising mode. Section V outlines our controller design strategy. Experimental results demonstrating the robot's performance in various scenarios are presented and analyzed in Section VI. Finally, Section VII concludes the paper.

II. MECHANICAL DESIGN

A. System Overview

The prototype comprises a quadcopter with an added wheel structure as shown in Fig. 1(a). The customized quadcopter was constructed from a flight control board (Bitcraze Crazyflie Bolt 1.1), four brushless motors (1104 7500KV), 2.5-inch propellers, a battery (900 mAh), and a carbon fiber airframe. Without an additional actuator for the wheel, an optical flow sensor suite (Bitcraze, Flow deck v2) supplements the onboard IMU for altitude and velocity measurements.

To achieve ground locomotion, we incorporated a passively hinged leg with a wheel. Mounted underneath the quadcopter, the leg features a passive single-degree-of-freedom revolute joint, allowing the rotation in the longitudinal plane. Two

bearings were adopted to reduce the joint friction. The rotation angle $\gamma \in [-10°, 40°]$ (measured with respect to the vertical direction) is limited by physical joint stoppers. This permits the wheel to be directly under ($\gamma = -10°$) or behind ($\gamma = 40°$) the robot's center of mass when it is on the ground, as illustrated in Fig. 1(b) and (c).

Unlike several designs with two or more larger wheels [17]–[19], the proposed wheel-leg structure is light. For the total mass of 196 g, the 21-g leg structure constitutes only approximately 10% of the total weight. This significantly reduces the dead weight during flight.

B. Hybrid Locomotion, Coordinates, and Configuration

In the aerial mode, the robot functions identically to conventional quadcopters. For the terrestrial mode, we distinguish two configurations: standing mode and cruising, corresponding to the wheel being in front of/behind according to the revolute joint state.

To describe those conditions geometrically, we introduce coordinate systems: the world frame $X_wY_wZ_w$ and the body-fixed frame $X_bY_bZ_b$ located at Center of Mass (CoM) of the robot as shown in Fig. 1(a). A rotation matrix R, relating the body frame to the world frame via ZYX Euler angles: roll ϕ, pitch θ, and yaw ψ, can be expressed using directional vectors of the body frame as $R = [X_b, Y_b, Z_b]$.

As illustrated in Fig. 2, the leg joint is located below and behind the CoM by distances d_v and d_h. We let d_l denote the leg's length. While standing, the front stopper positions the wheel directly below the CoM (Fig. 2(b)). To keep the stopper engaged, the joint is placed slightly behind the CoM ($d_v = 12$ mm), allowing ground normal force to apply torque, pressing the leg against the stopper. This occurs when the robot is upright, with most of its weight supported by ground reaction force, resulting in an efficient configuration. Standing is ideal for static applications like prolonged environmental monitoring.
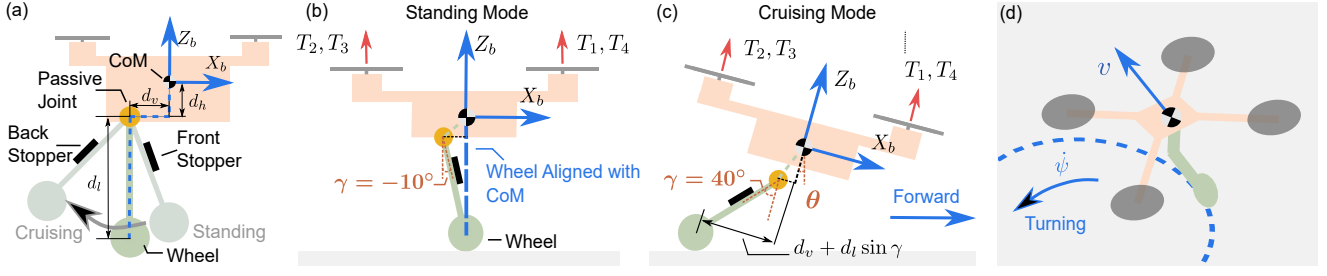
Fig. 2. Leg configurations in different operating modes. (a) Dimensions and kinematics of the leg and joint stoppers. The angle γ measures the leg angle l with respect to Y_b. The standing mode engages the front stopper ($\gamma = -10°$) whereas the cruising mode relies on the back stopper ($\gamma = 40°$). (b) Standing mode. The wheel and the CoM are aligned with Z_b. (c) Cruising mode. (d) Motion of the robot while cruising, with the forward speed v and turning rate $\dot{\psi}$.

On the other hand, cruising on the ground makes use of the other stopper ($\gamma = 40°$). As presented in Fig. 2(c), the wheel is positioned behind the CoM.

To capture the difference between the two configurations, we define a leg vector to represent the ground contact point in the body frame:

$$l = \begin{bmatrix} -d_v - d_l \sin\gamma & 0 & -d_h - d_l \cos\gamma \end{bmatrix}^T, \quad (1)$$

with $d_v = 12$ mm, $d_h = 30$ mm, $d_l = 70$ mm. In the standing configuration ($\gamma = -10°$), the leg vector passes through the CoM and is parallel to Z_B as $-d_v + d_l \sin(10°) = 0$. At $\gamma = 40°$, the component $-d_v - d_l \sin\gamma$ becomes -57 mm, meaning the wheel is located 57 mm behind the CoM. This distance was found to provide satisfactory passive yaw stability during ground locomotion while keeping the robot compact.

III. AERIAL AND TERRESTRIAL DYNAMICS

Unlike in aerial operations, the robot interacts with the ground in its terrestrial mode. We define a boolean variable:

$$\beta = \begin{cases} 0 & \text{Aerial mode} \\ 1 & \text{Terrestrial mode} \end{cases}, \quad (2)$$

such that the equations of motion in both operational modes can be readily differentiated.

A. Translational and Attitude Dynamics

Define p as the position of the robot in the inertial frame, mg as the robot's weight, and the total thrust in the body frame as Te_3^b ($e_3 = [0, 0, 1]^T$ is a basis vector), we yield

$$m\ddot{p} = -mge_3 + RTe_3 + \beta(F_N e_3 - F_f), \quad (3)$$

where the force terms on the right hand side includes the ground reaction force F_N and friction F_f which only appear in the terrestrial mode.

Regardless of the operational mode, (3) states that the horizontal acceleration (first two elements of $\ddot{p}$) is influenced by the thrust vector RTe_3. On the ground, friction may become significant, in particular in the direction along the wheel axle $\pm Y_b$. Thanks to the non-holonomic constraints, it is more efficient for the robot to primarily move in the longitudinal (forward) direction. Similar to its flight mode, the longitudinal acceleration of the robot is approximately dependent on the pitch angle as $T\sin\theta$. The longitudinal speed is controlled by regulating the pitch angle.

Meanwhile, the attitude dynamics are governed by the propelling torque $\tau = [\tau_x, \tau_y, \tau_z]^T$ and torque induced from the ground reaction as well as friction. Therefore,

$$J\dot{\omega} = \tau - \omega \times J\omega + \beta \left(l \times R^T (F_N e_3 - F_f) \right), \quad (4)$$

where $J = \text{diag}(J_x, J_y, J_z)$ is the inertia (with off-diagonal terms neglected), $\omega = [\omega_x, \omega_y, \omega_z]^T$ is the body-centric angular velocity, and the term $l\times$ accounts for the location and direction of the respective forces with respect to the CoM of the robot. Combining (3) with (4) allows us to eliminate the term $F_N - F_f$ to produce

$$J\dot{\omega} = \tau - \omega \times J\omega + \beta \left(l \times R^T (m\ddot{p} + mge_3 - RTe_3) \right), \quad (5)$$

independent of friction and ground reaction force.

B. Simplified Ground Dynamics

As the flight dynamics of the robot is indistinguishable from a regular quadrotor, in this work, we focus on the wheeled locomotion. To obtain a tractable model for control purposes, we incorporate the following simplifying assumptions.

First, in addition to the non-holonomic constraints, we assume the robot cruises on the ground with a constant forward speed v while turning at a constant rate $\dot{\psi}$, as depicted in Fig. 2(d). In other words, we assume the acceleration of the robot is only non-zero along its lateral direction ($Y_b^T \ddot{p} \neq 0$, whereas $X_b^T \ddot{p}, Z_b^T \ddot{p} = 0$). As a consequence, the term $R^T \ddot{p} = [X_b^T \ddot{p}, Y_b^T \ddot{p}, Z_b^T \ddot{p}]^T$ in (5) becomes $[0, Y_b^T \ddot{p}, 0]^T$. As a result, the cross product $l \times R^T \ddot{p}$ reduces to $[Y_b^T \ddot{p}(d_h + d_l \cos\gamma), 0, -Y_b^T \ddot{p}(d_v + d_l \sin\gamma)]^T$.

Second, to minimize the coupling between the roll, pitch, and yaw axes, we assume $\omega_x, \omega_y \approx 0$ such that the term $\omega \times J\omega$ in (5) is negligible.

Third, based on preliminary experiments, the pitch angle of the robot remains small (below $10°$) even when the forward speed of the robot reaches 2 m/s. This allows us to assume the pitch angle θ is zero when we deal with the contribution from the robot's weight mg in (5) to analyze the roll and yaw dynamics. Similarly, we assume the roll angle ϕ to be zero to simplify the pitch dynamics.

Together, these reduce the combined dynamics from (5) to:

$$J_x \frac{d\dot\phi}{dt} = \tau_x + \beta \left(mg(d_h + d_l \cos\gamma)\sin\phi \right. \tag{6}$$
$$\left. + m\boldsymbol{Y}_b^T \ddot{\boldsymbol{p}}(d_h + d_l \cos\gamma) \right)$$

$$J_y \frac{d\dot\theta}{dt} = \tau_y + \beta \left(-T(d_v + d_l \sin\gamma) \right. \tag{7}$$
$$\left. + mg \left((d_v + d_l \sin\gamma)\cos\theta + (d_h + d_l \cos\gamma)\sin\theta \right) \right)$$

$$J_z \frac{d\dot\psi}{dt} = \tau_z + \beta \left(-mg(d_v + d_l \sin\gamma)\sin\phi \right. \tag{8}$$
$$\left. - m\boldsymbol{Y}_b^T \ddot{\boldsymbol{p}}(d_v + d_l \sin\gamma) \right),$$

where we have used $\dot\phi$, $\dot\theta$, and $\dot\psi$ to represent body-centric angular velocities, consistent with other simplifying assumptions. Furthermore, as a non-holonomic system, the lateral acceleration terms in (6) and (8), corresponding to the centrifugal acceleration, can be expressed as

$$\boldsymbol{Y}_b^T \ddot{\boldsymbol{p}} = v\dot\psi. \tag{9}$$

The tractable model derived here subsequently informs us about the advantages of the proposed leg design, serving as the foundation for the development of suitable control strategies.

IV. BENEFITS OF RECONFIGURABLE LEG DESIGN

The reconfigurable leg design of our robot offers significant advantages in both standing and cruising modes. This section explores these benefits, focusing on the robot's ability to stand with minimal effort, achieve passive yaw rate stability during cruising, and maintain enhanced robustness on uneven terrain.

A. Standing with Minimal Effort

Some benefits of the leg joint stoppers can be seen in (7). In the standing mode $(d_v - d_l \sin(10°) = 0)$, the robot is in pitch equilibrium with zero pitch angle, no pitch torque, and minimal net thrust. This allows the robot to stand with minimal effort. However, this configuration makes the robot susceptible to yaw disturbances when it traverses on the ground as elaborated below. The reconfigurable leg permits the robot to be versatile for both standing and cruising tasks.

B. Passive Yaw Rate Stability

In the cruising mode, the negative offset of the leg vector in (1) brings in passive yaw rate stability. This decreases the importance of precise yaw control when the robot travels at a high speed on the ground.

When the speed v and roll angle ϕ of the robot are constant, the yaw dynamics in (8) and (9), in the absence of yaw torque $(\tau_z = 0)$, can be written as:

$$J_z \ddot\psi + mv(d_v + d_l \sin\gamma)\left(\dot\psi + g\sin\phi/v\right) = 0, \tag{10}$$

which states that the yaw rate passively converges to a value determined by ϕ according to $\dot\psi \to -g\sin\phi/v$. For instance, when $\phi = 0$, we obtain $\dot\psi \to 0$.

This passive yaw rate stability brings two important implications. First, it allows the turning rate to be controlled by the roll angle rather than directly through τ_z. This substantially
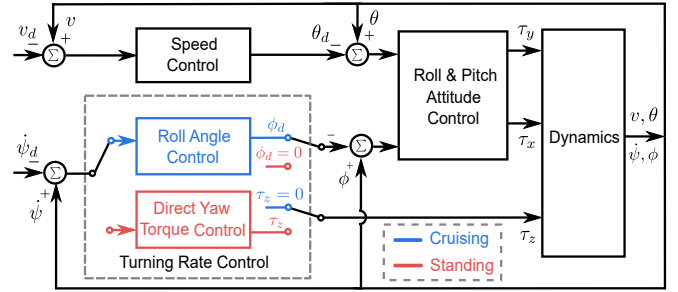

Fig. 3. Block diagram outlining the structure of the controller for the terrestrial mode. The yaw controller for the standing and cruising modes are different.

enhances the achievable turning rate as elaborated below. Second, passive stability improves robustness when the robot travels on less even terrains, as we explain below.

C. Enhanced Robustness on Uneven Terrain

In practice, we find that the passive yaw rate stability substantiated by (10) notably improves the robustness of the robot in experiments, preventing the robot from crashing when traveling on non-smooth grounds, as shown later in Section VI-C1. This observation can be explained by the combined dynamics in (6)-(8). That is, the yaw rate instability could cause an instability in the roll dynamics, leading to crashes.

Consider an impulsive yaw torque disturbance that leads to an abrupt change in the yaw angle ψ; this rapidly reorients the heading direction of the robot (a sudden turn), affecting the directions of $\boldsymbol{X}_b$ and $\boldsymbol{Y}_b$. Meanwhile, the acceleration of the robot $\ddot{\boldsymbol{p}}$ in the inertial frame remains unchanged in this short time period. This implies the centrifugal term, $m\boldsymbol{Y}_b^T \ddot{\boldsymbol{p}}(d_h + d_l \cos\gamma)$, in the roll dynamics or (6) is suddenly altered. As the change could be too abrupt and dramatic for the controller, this leads to roll instability, causing the robot to crash.

While the use of active yaw control through τ_z could theoretically alleviate this issue, in practice, sudden yaw disturbances could easily overcome the correction torque generated by the controller as illustrated in the experiments (Section VI-A). Furthermore, a high net thrust is required to produce large yaw torque. This may undesirably cause the robot to liftoff from the ground.

V. CONTROLLER DESIGN

Our controller design applies a cascaded structure comprising inner loop attitude controllers and outer loop motion controllers, tailored for both aerial and terrestrial modes. This section details the control strategies employed for each mode, including the approaches for aerial motion control, terrestrial speed and turning rate control, roll and pitch control, and the transition mechanisms between these modes.

A. Aerial Motion Control

During flight, the outer loop controller relies on feedback from the optical flow sensor (Bitcraze, Flow deck v2) to control its ground speed and attitude. The altitude and velocity setpoints are either predefined or directly commanded by an

operator. The altitude error is translated into the total thrust command and the velocity error is used to compute the desired roll and pitch angles for the low-level controller. The onboard attitude controller then generates individual motor commands based on the setpoint and the IMU feedback.

B. Terrestrial Mode Control

In the terrestrial mode, the robot is controlled to realize the desired speed v_d and turning rate $\dot{\psi}_d$. This is achieved by the outer loop controller, which determines the setpoint for the inner attitude controller. The overall framework is shown in Fig. 3 and elaborated below.

1) Speed Controller: As described in Section III-A, the acceleration of the robot in the longitudinal direction is approximately subject to $T\sin\theta$ and friction. We employ a proportional-integral controller to evaluate the pitch angle setpoint that stabilizes the speed of the robot according to

$$\theta_d = -k_{v,p}(v - v_d) - k_{v,i}\int(v - v_d)\mathrm{d}t, \quad (11)$$

in which $k_{(\cdot),(\cdot)}$'s are controller gains. We assume that the change of T is small during our experiments. The use of the integral term deals with uncertainties, allowing us to approximate $T\sin\theta$ as θ (treating T as a constant) and deal with the influence of friction without an explicit model.

2) Turning Rate Controller: Unlike the speed controller, turning is separately considered for the ground locomotion in the standing and cruising configurations.

In the standing mode, the yaw dynamics described by (8) simplifies to $J_z\ddot{\psi} = \tau_z$, identical to the aerial mode, as $-d_v + d_l\sin(10°) = 0$. Therefore, the yaw rate is controlled through the use of induced torque differentially generated by clockwise-spinning and counterclockwise-spinning propeller pairs as typically implemented in multirotor robots.

For the cruising mode, the proposed leg configuration allows the turning rate to be effectively controlled through the roll angle with $\tau_z = 0$ as explained in Section IV. To accommodate a non-constant yaw rate setpoint $\dot{\psi}_d$, the desired roll angle is computed based on (10) as

$$\sin\phi_d = k_{\dot{\psi}}(\dot{\psi} - \dot{\psi}_d) - \frac{v\dot{\psi}}{g} - \frac{J_z\ddot{\psi}_d}{mg(d_v + d_l\sin\gamma)}, \quad (12)$$

resulting in stable closed-loop dynamics:

$$J_z(\ddot{\psi} - \ddot{\psi}_d) + k_{\dot{\psi}}mg(d_v + d_l\sin\gamma)(\dot{\psi} - \dot{\psi}_d) = 0. \quad (13)$$

3) Roll and Pitch Control: The same control strategy for roll and pitch angles applies for both aerial and terrestrial modes. Given the roll setpoint ϕ_d from the high-level or turning rate controller, the control law for roll torque is

$$\begin{aligned}\tau_x =& \ddot{\phi}_d - k_{\phi,d}\left(\dot{\phi} - \dot{\phi}_d\right) - k_{\phi,p}(\phi - \phi_d) \\ &- \beta\Big(mg(d_h + d_l\cos\gamma)\sin\phi \\ &+ mv\dot{\psi}(d_h + d_l\cos\gamma)\Big),\end{aligned} \quad (14)$$

such that, when taking into account (6) and (9), we yield stable closed-loop dynamics: $(\ddot{\phi} - \ddot{\phi}_d) + k_{\phi,d}(\dot{\phi} - \dot{\phi}_d) + k_{\phi,p}(\phi - \phi_d) = $

0. Notice that in the ground mode, it is essential to compensate for the torque contributed by the robot's weight (when the pitch angle is non zero) and the centrifugal acceleration.

Likewise, for the setpoint θ_d provided by the speed controller in (11), the pitch command is

$$\begin{aligned}\tau_y =&\ddot{\theta}_d - k_{\theta,d}(\dot{\theta} - \dot{\theta}_d) - k_{\theta,p}(\theta - \theta_d) - \beta\left(-T(d_v + d_l\sin\gamma)\right. \\ &\left.+ mg\left(d_v + d_l\sin\gamma\right)\cos\theta + (d_h + d_l\cos\gamma)\sin\theta\right)),\end{aligned} \quad (15)$$

resulting in stable closed-loop dynamics when (7) is considered. To deal with the presence of T in the control law, we propose the following thrust allocation method.

4) Motor Thrust Allocation: In terrestrial mode, the robot primarily requires torque for trajectory tracking and attitude stabilization, with thrust mainly used for torque generation. Based on this and the pitch control law (15), we modify the allocation scheme as follows. Starting from a mapping of the aerial mode:

$$\begin{bmatrix} \tau_x & \tau_y & \tau_z & T \end{bmatrix}^T = \boldsymbol{A}\boldsymbol{T}, \quad (16)$$

where $\boldsymbol{A}$ is a matrix corresponding to the robot's geometry and aerodynamic coefficients of the thrusters and $\boldsymbol{T}$ is a vector containing individual thrusts $[T_1, T_2, T_3, T_4]^T$. We perform row operations on (16) and eliminate the last row to yield

$$\begin{bmatrix} \tau_x & \tau_y - T(d_v + d_l\sin\gamma) & \tau_z \end{bmatrix}^T = \boldsymbol{B}\boldsymbol{T}, \quad (17)$$

where we have regarded $d_v + d_l\sin\gamma$ as a constant and modified the mapping matrix from $\boldsymbol{A}$ to $\boldsymbol{B}$ accordingly. Herein, the term $\tau_y - T(d_v + d_l\sin\gamma)$ is directly taken from the control law in (15) and $\boldsymbol{B}$ is 3×4.

As an underdetermined system, $\boldsymbol{T}$ can be solved from

$$\begin{aligned}\boldsymbol{T} =& \boldsymbol{B}^+\begin{bmatrix} \tau_x & \tau_y - T(d_v + d_l\sin\gamma) & \tau_z \end{bmatrix}^T \\ &+ \left(\boldsymbol{I} - \boldsymbol{B}^+\boldsymbol{B}\right)\xi,\end{aligned} \quad (18)$$

where $\boldsymbol{B}^+$ represents a pseudoinverse of $\boldsymbol{B}$, $(\boldsymbol{I} - \boldsymbol{B}^+\boldsymbol{B})$ is an orthogonal projection matrix that projects onto the null space of $\boldsymbol{B}$, and a scalar ξ can be chosen such that elements of $\boldsymbol{T}$ are non-negative [23].

C. Mode Transitions

The transitions between aerial and terrestrial modes occur during the take-off and landing procedures. To land, the thrust command is gradually reduced. After the robot drops below 20 cm (based on feedback from the optical flow sensor), the robot is provided with a small positive or negative ($\pm 8°$) pitch angle setpoint. This conditions the robot to eventually be in standing mode ($\gamma = -10°$) or cruising ($\gamma = 40°$), respectively, after landing. The ground contact is determined by monitoring the vertical acceleration using the onboard IMU.

VI. EXPERIMENTAL VALIDATION

Herein, we conducted both indoor and outdoor experiments to validate the performance of the robot, focusing on its terrestrial mode and highlighting the benefits of passive yaw rate stability. For the indoor tests, we planned nominal speed and turning rate setpoints from the desired trajectory. A motion
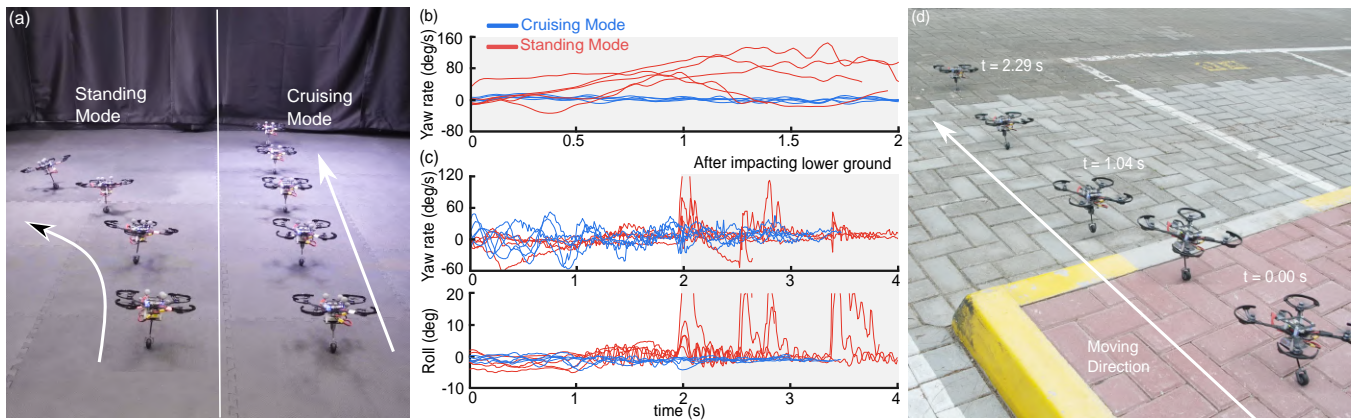
Fig. 4. Passive yaw rate stability and robust maneuvers. (a) The robot with a leg fixed in the standing mode and a leg in the cruising mode. The former struggled to maintain its heading despite employing active yaw control, whereas the latter traveled in a straight line without active yaw control. (b) Plot of the yaw rate from both configurations in (a) (five trials each). (c) Plot of the yaw rate and roll angles for the outdoor tests (five trials each). The robot made an impact on the lower ground at $t = 2$ s. (d) A composite photo showing the robot cruising down a 10-cm step without losing its stability.

capture system provides position feedback, and we use a method from [24] (developed for wheeled non-holonomic robots) to compute the actual speed and turning rate setpoints based on the position error in real-time. For the outdoor tests, we provided the speed and turning rate setpoints to the robot.

A. Passive Yaw Rate Stability for the Cruising Mode

As manifested by (10), the longitudinal offset of the leg vector of the robot in the cruising mode contributes to yaw rate stability. Here, we experimentally verified this stability by commanding the robot in the cruising mode ($40°$) to travel at a constant speed of $v = 1.5$ m/s with $\phi_d = 0°$ and zero yaw torque for around 2.0 s. As a benchmark, the robot with the leg fixed at the standing mode configuration was instructed to perform the same task. Five repeated trials were conducted. Fig. 4(a) exemplifies the outcomes, accompanied by the recorded yaw rate in Fig. 4(b).

Overall, the results confirm the expected stable yaw rate of $0°$ deg/s for the robot in the cruising mode. The benchmark robot illustrates visible variations in the yaw rate when disturbed by uneven ground, slippage, etc. The Root Mean Square (RMS) values of $\dot{\psi}$ of both robots are 80 and 6 deg/s, implying that the proposed leg design results in robustness against disturbances and surface irregularities, simplifying the need for complex active yaw control.

B. Terrestrial Trajectory Tracking

With the position feedback from the motion capture system, we conducted terrestrial trajectory tracking experiments of the robot in the cruising mode. The robot was nominally provided with different setpoint speed v_d and roll angles ϕ_d. The instantaneous setpoints varied slightly to correct for current tracking errors [24].

First, the robot tracked a circular trajectory with a radius of 0.57 m (nominally $v_d = 1$ m/s and $\dot{\psi}_d = 100$ deg/s, Fig. 5(a)). On average, the robot traveled at a speed of 1.19 m/s while turning at a rate of 91 deg/s, achieving a normalized centrifugal acceleration $\bar{a}_c = v\dot{\psi}/g$ of 0.20. Within 10 s, the

robot traveled over 11.9 m, with the RMS position error of only 2 cm. During this period, the RMS values of $v - v_d$ and $\dot{\psi} - \dot{\psi}_d$ are 0.15 m/s and 26 deg/s.

We repeated the experiment at a faster speed and more aggressive turning rate. The robot was instructed to track a circle of radius 1.19 m nominally at a speed of 2.6 m/s and yaw rate of 125 deg/s. In this case, the robot traveled over 29.5 m in 10 s, recording an average speed and turning rate of 2.98 m/s and 103 deg/s. It achieved the RMS position error of 11 cm, RMS value of $v - v_d$ of 0.41 m/s, and RMS value of $\dot{\psi} - \dot{\psi}_d$ of 26 deg/s. The robot recorded a normalized centrifugal acceleration of 0.55 on average, higher than other robots as depicted in Fig. 1(e).

Comparing the tracking performance to other aerial robots capable of rolling, our results are competitive. The tracking error in [19] was 12 cm for a trajectory with a maximum speed of 2.9 m/s, The robot in [21] achieved a slightly lower error of 8 cm with an average speed of 3.3 m/s, and in [18], the work recorded a tracking error of 11 cm for a maximum speed of 3.0 m/s. Hence, we demonstrate a comparable RMS position error at a similar speed, but with a higher normalized centrifugal acceleration.

Moreover, we evaluated the robot's turning-in-place capability in cruising mode by commanding a setpoint speed of zero and various yaw rates. For yaw rates below 125 deg/s, the robot executed smooth turns with minimal translation. At higher rates around 150 deg/s, the robot exhibited a circular trajectory with a radius of $\approx$2 cm (measured at the wheel) while yawing. When commanded to turn faster than 180 deg/s, the robot could no longer maintain its position. These results show that the robot can also achieve moderate turning rates while staying stationary.

C. Outdoor Experiments

We also operated the robot outdoors using onboard optical flow and time-of-flight sensors instead of offboard feedback. We employed an FPV camera package (Zenchansi, 5.6 g) to simulate a surveillance application.
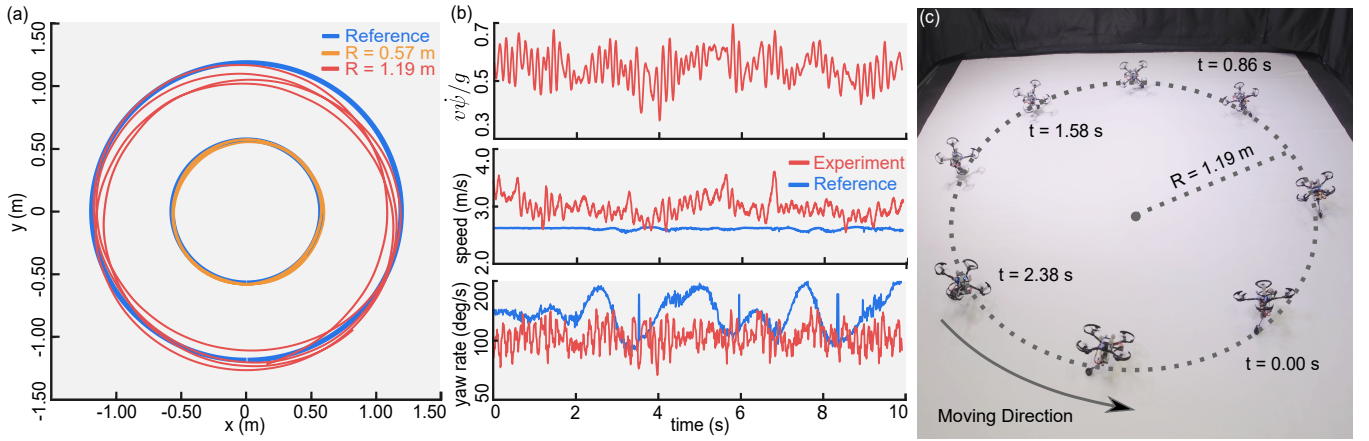
Fig. 5. Indoor trajectory tracking in the cruising mode. (a) Trajectories from two tests. (i) A circular trajectory with a radius of 0.57 m. The robot accurately tracked this with the average speed and turning rate of 1.0 m/s and 100 deg/s. (ii) A circular trajectory with a radius of 1.19 m. The robot tracked this with the average speed and turning rate of 2.6 m/s and 125 deg/s. At a higher speed and turning rate, the normalized centrifugal acceleration reached 0.55 on average, resulting in a slightly elevated tracking error. (b) Measured speed, yaw rate, and normalized centrifugal acceleration from the larger circular trajectory. (c) A composite photo when the robot tracked the circular trajectory with a 1.19-m radius.
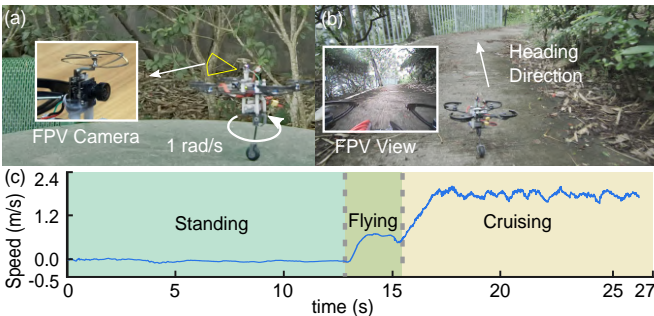

Fig. 6. Outdoor experiment. (a) The robot started in standing mode on an elevated surface. It yawed at a rate of 1 rad/s to observe the surroundings via an FPV camera. (b) Thereafter, the robot took off and landed on the ground in the cruising mode. It then traversed forward at 1.8 m/s. (c). The speed measurement from the optic flow-based estimator encompassing the entire period. When flying, the flight speed was approximately 0.5 m/s.

1) Traveling through a Step: First, we operated the robot in cruising mode at 1 m/s and zero yaw rate over a 10-cm drop. As shown in Fig. 4(d), after impact with the lower ground, the robot continued stably without crashing. We repeated the test five times with a 100% success rate. The recorded yaw rate showed little variation (Fig. 4(c)). For comparison, we repeated the test with the leg fixed in standing mode and active yaw control. Initially, the robot maintained a low yaw rate (Fig. 4(c)), but became unstable after transitioning to the lower ground, often lifting off (due to the attempt to generate large yaw torque, resulting in excessive thrust) or crashing (as indicated by roll errors in Fig. 4(c)). These results highlight the role of passive yaw stability in handling uneven terrain.

2) Multimodal Trajectory: As depicted in Fig. 6(a), the robot started on an elevated surface in the standing mode, performing surveillance by yawing at 1 rad/s. In this mode, the yaw torque is generated via the propellers' induced torque as described in Section V-B2. After 12 s, the robot took off, landed on concrete in cruising mode, and transitioned to ground locomotion upon detecting ground contact via the

accelerometer. It then tracked a constant speed of $v = 1.8$ m/s as seen in Fig. 6(b) and the Supplementary Video. Onboard estimates in Fig. 6(c) confirm the robot maintained an approximate speed of 1.8 m/s.

D. Power Consumption and Cost of Transport

We measured power consumption by recording battery voltage from the flight control board's sensor and current from the ESCs. Average power was calculated over one minute. The resting power of the electronics without actuation is 3.4 W.

Over different operating modes, the robot consumed the least power while standing (16.5 W). In low-speed cruising, the power consumption approximately doubles, with the difference between 0.5 m/s and 1.0 m/s speeds being minimal. These were measured using a circular trajectory with a radius of 0.6 m. When flying at similar speeds (0.5 m/s and 1.0 m/s), the power consumptions of 66.4 W and 69.1 W were also approximately twice as high as cruising, indicating the power saving benefit of cruising at low speeds.

This power consumption pattern is closely linked to the thrust requirements in each mode. While standing, the robot generates an average thrust of 34.7 gf ($0.18mg$). As the robot begins cruising at 0.5 m/s, the average thrust increases to 83.7 gf ($0.43mg$). At a cruising speed of 1.0 m/s, the average thrust further rises to 95.7 g or $0.49mg$. These increasing thrust demands explain the doubling in power consumption between standing and cruising.

In addition, we calculated the normalized energy consumption per unit distance, known as the Cost of Transport (COT). When flying at 1.0 m/s, the COT was 36.0, compared to 17.4 while cruising at the same speed. This indicates that the robot can travel nearly twice the distance when cruising, highlighting the significant energy efficiency of cruising at low speeds over flying.

We also evaluated the energy impact of the added leg mechanism by comparing hovering flight power consumption.

The robot consumed 66.1 W with the leg attached and 61.9 W without it. This small difference of 4.2 W (6%) demonstrates that our lightweight leg design has minimal impact on the robot's flight power requirements.

To validate our power measurements, we performed an endurance test, comparing hovering flight and standing. The robot achieved a standing duration of 1052 seconds, which was 3.8 times longer than its hovering duration of 274 seconds. This ratio closely matches the 4.0 power ratio between hovering and standing.

E. Power and Structural Efficiency

Compared with other air-ground robots, we analyze both power saving efficiency and structural efficiency as defined in [21]. The power saving efficiency represents the reduction in power consumption during ground locomotion compared to aerial mode, after accounting for standby power. Our design demonstrates an efficiency of 53.5%, which is lower than Skywalker (85.8%) [21] and Skater (85.8%) [19]. This relatively lower efficiency is a direct consequence of the wheeled leg design.

The structural efficiency, defined as the proportion of mass not dedicated to ground locomotion mechanisms, reaches 89.3% in our design. This is higher than Skywalker (82.4%) [21] but lower than Skater (93.7%) [19]. The relatively high structural simplicity stems from our minimalist passive leg design, which adds minimal weight while enabling robust ground maneuverability.

VII. Conclusion

In summary, we presented a hybrid quadrotor design with a passively reconfigurable wheeled leg for robust terrestrial maneuvers. The unique leg configuration provides several key advantages—upright standing with reduced effort, passive yaw stability during cruising for improved robustness on uneven terrain, and aggressive steering by controlling yaw through roll rather than induced torque. Through indoor and outdoor experiments, we validated the effectiveness of the proposed design and control methods, achieving stable maneuvers on uneven terrains and tight turns at high speeds. While our design achieves excellent maneuverability and robustness, it demonstrates lower power efficiency compared to state-of-the-art air-ground robots that use dedicated driving mechanisms. This highlights an inherent trade-off in our approach.

References

[1] K. Dong, R. Ding, S. Bai, X. Cai, and P. Chirarattananon, "Stabilizing aerodynamic dampers for cooperative transport of a suspended payload with aerial robots," *Advanced Intelligent Systems*, vol. 5, no. 9, p. 2300112, 2023.

[2] G. Hardouin, J. Moras, F. Morbidi, J. Marzat, and E. M. Mouaddib, "A multirobot system for 3-d surface reconstruction with centralized and distributed architectures," *IEEE Transactions on Robotics*, 2023.

[3] W. Tabib, K. Goel, J. Yao, C. Boirum, and N. Michael, "Autonomous cave surveying with an aerial robot," *IEEE Transactions on Robotics*, vol. 38, no. 2, pp. 1016–1032, 2021.

[4] Y. Mulgaonkar, M. Whitzer, B. Morgan, C. M. Kroninger, A. M. Harrington, and V. Kumar, "Power and weight considerations in small, agile quadrotors," in *Micro-and Nanotechnology Sensors, Systems, and Applications VI*, vol. 9083. SPIE, 2014, pp. 376–391.

[5] R. Ding, S. Bai, K. Dong, and P. Chirarattananon, "Aerodynamic effect for collision-free reactive navigation of a small quadcopter," *npj Robotics*, vol. 1, no. 1, p. 2, 2023.

[6] A. Fabris, E. Aucone, and S. Mintchev, "Crash 2 squash: An autonomous drone for the traversal of narrow passageways," *Advanced Intelligent Systems*, vol. 4, no. 11, p. 2200113, 2022.

[7] C. J. Pratt and K. K. Leang, "Dynamic underactuated flying-walking (duck) robot," in *2016 IEEE International Conference on Robotics and Automation (ICRA)*. IEEE, 2016, pp. 3267–3274.

[8] Y. Mulgaonkar, B. Araki, J.-s. Koh, L. Guerrero-Bonilla, D. M. Aukes, A. Makineni, M. T. Tolley, D. Rus, R. J. Wood, and V. Kumar, "The flying monkey: A mesoscale robot that can run, fly, and grasp," in *2016 IEEE International Conference on Robotics and Automation (ICRA)*, 2016, pp. 4672–4679.

[9] S. Bai, Q. Pan, R. Ding, H. Jia, Z. Yang, and P. Chirarattananon, "An agile monopedal hopping quadcopter with synergistic hybrid locomotion," *Science Robotics*, vol. 9, no. 89, p. eadi8912, 2024.

[10] K. Kim, P. Spieler, E.-S. Lupu, A. Ramezani, and S.-J. Chung, "A bipedal walking robot that can fly, slackline, and skateboard," *Science Robotics*, vol. 6, no. 59, p. eabf8136, 2021.

[11] A. Kalantari, T. Touma, L. Kim, R. Jitosho, K. Strickland, B. T. Lopez, and A.-A. Agha-Mohammadi, "Drivocopter: A concept hybrid aerial/ground vehicle for long-endurance mobility," in *2020 IEEE Aerospace Conference*. IEEE, 2020, pp. 1–10.

[12] N. B. David and D. Zarrouk, "Design and analysis of fcstar, a hybrid flying and climbing sprawl tuned robot," *IEEE Robotics and Automation Letters*, vol. 6, no. 4, pp. 6188–6195, 2021.

[13] E. Sihite, A. Kalantari, R. Nemovi, A. Ramezani, and M. Gharib, "Multi-modal mobility morphobot (m4) with appendage repurposing for locomotion plasticity enhancement," *Nature communications*, vol. 14, no. 1, p. 3323, 2023.

[14] D. Hu, R. Xia, X. Jin, and Y. Tang, "Trajectory planning and tracking of hybrid flying-crawling quadrotors," *arXiv preprint arXiv:2312.08718*, 2023.

[15] M. Cao, X. Xu, S. Yuan, K. Cao, K. Liu, and L. Xie, "Doublebee: A hybrid aerial-ground robot with two active wheels," in *2023 IEEE/RSJ International Conference on Intelligent Robots and Systems (IROS)*. IEEE, 2023, pp. 6962–6969.

[16] A. Kalantari and M. Spenko, "Design and experimental validation of hytaq, a hybrid terrestrial and aerial quadrotor," in *2013 IEEE International Conference on Robotics and Automation*. IEEE, 2013, pp. 4445–4450.

[17] H. Jia, R. Ding, K. Dong, S. Bai, and P. Chirarattananon, "Quadrolltor: a reconfigurable quadrotor with controlled rolling and turning," *IEEE Robotics and Automation Letters*, 2023.

[18] R. Zhang, J. Lin, Y. Wu, Y. Gao, C. Wang, C. Xu, Y. Cao, and F. Gao, "Model-based planning and control for terrestrial-aerial bimodal vehicles with passive wheels," in *2023 IEEE/RSJ International Conference on Intelligent Robots and Systems (IROS)*. IEEE, 2023, pp. 1070–1077.

[19] J. Lin, R. Zhang, N. Pan, C. Xu, and F. Gao, "Skater: A novel bi-modal bi-copter robot for adaptive locomotion in air and diverse terrain," *IEEE Robotics and Automation Letters*, vol. 9, no. 7, pp. 6392–6399, 2024.

[20] J. Gao, H. Jin, L. Gao, J. Zhao, Y. Zhu, and H. Cai, "A multimode two-wheel-legged land-air locomotion robot and its cooperative control," *IEEE/ASME Transactions on Mechatronics*, 2023.

[21] N. Pan, J. Jiang, R. Zhang, C. Xu, and F. Gao, "Skywalker: A compact and agile air-ground omnidirectional vehicle," *IEEE Robotics and Automation Letters*, vol. 8, no. 5, pp. 2534–2541, 2023.

[22] Z. Zheng, J. Wang, Y. Wu, Q. Cai, H. Yu, R. Zhang, J. Tu, J. Meng, G. Lu, and F. Gao, "Roller-quadrotor: A novel hybrid terrestrial/aerial quadrotor with unicycle-driven and rotor-assisted turning," in *2023 IEEE/RSJ International Conference on Intelligent Robots and Systems (IROS)*. IEEE, 2023, pp. 6927–6934.

[23] H. Jia, S. Bai, and P. Chirarattananon, "Aerial manipulation via modular quadrotors with passively foldable airframes," *IEEE/ASME Transactions on Mechatronics*, vol. 28, no. 4, pp. 1930–1938, 2023.

[24] Z.-P. Jiang, E. Lefeber, and H. Nijmeijer, "Saturated stabilization and tracking of a nonholonomic mobile robot," *Systems & Control Letters*, vol. 42, no. 5, pp. 327–332, 2001.